Quantitating drug-target engagement in single cells *in vitro* and *in vivo*

J Matthew Dubach[1], Eunha Kim[1,3], Katherine Yang[1], Michael Cuccarese[1], Randy J Giedt[1], Labros G Meimetis[1], Claudio Vinegoni[1] & Ralph Weissleder[1,2]

Quantitation of drug target engagement in single cells has proven to be difficult, often leaving unanswered questions in the drug development process. We found that intracellular target engagement of unlabeled new therapeutics can be quantitated using polarized microscopy combined with competitive binding of matched fluorescent companion imaging probes. We quantitated the dynamics of target engagement of covalent BTK inhibitors, as well as reversible PARP inhibitors, in populations of single cells using a single companion imaging probe for each target. We then determined average *in vivo* tumor concentrations and found marked population heterogeneity following systemic delivery, revealing single cells with low target occupancy at high average target engagement *in vivo*.

To achieve the desired biological response, drugs must first reach the intended organ or tissue, enter the cell (for intracellular proteins), and engage the target[1]. The duration, completeness and cellular heterogeneity of drug-target engagement dictate success. Most pharmacokinetic studies rely on bulk sampling of plasma or tissue providing modest information on drug activity at the cellular target. Furthermore, new mechanistic targets are not easily invalidated in failed treatments if target engagement was not confirmed, which, for example, was the case in 43% of phase II failures in a recent study[2]. Given the complexity of *in vivo* drug action[3], and recent clinical failures of drugs that were not properly characterized[4], methods to determine cellular drug binding could, in theory, reduce the considerable clinical failure rates and associated high costs.

Direct chemical modification of drugs can attach small labels such as biotin or fluorophores, enabling tissue distribution and target engagement measurements by pull-down assays or imaging[5–8]. However, the addition of a label changes the physiochemical properties of a small molecule, and the results may not be directly relevant to the parent drug candidate. Conversely, labeling target proteins with genetic fluorescent labels, such as GFP, may alter protein activity or trafficking[9]. Out of several creative label-free approaches to measure target engagement[10–12], PET imaging is currently the most commonly used at multiple stages in drug development[13]. Radiolabeled drug measures tissue accumulation[14], whereas a lack of accumulation following drug administration is indicative of parent drug target occupancy[10]. However, this approach does not consider nonspecific accumulation[15], lacks single-cell spatial resolution and some radio-labels, such as carbon-11, have a limiting half-life[16]. Alternatively, the cellular thermal shift assay (CETSA) measures bound protein thermal stabilization to determine target engagement and can be extended to *in vivo* measurements[17]. However, CETSA yields cell population averages, and these results are difficult to quantitate, with *in vivo* measurements only being demonstrated with covalent drugs. Enzymatic drug inhibition can be measured using activity-based probes[18] or molecules that become fluorescent following enzyme cleavage[19]. Although these approaches provide valuable insight into target inhibition, they require reactive or cleavable

probes, are limited to certain protein classes and lack spatial resolution. Thus, measuring the engagement of clinical drug with the target at the cellular level and *in vivo* with reversible inhibitors has remained elusive.

We developed a new approach to quantifying target occupancy of unlabeled drugs at cellular resolution using competitive binding with fluorescently labeled companion imaging probes (CIPs) and fluorescence polarization microscopy. Our approach takes advantage of the target specificity of a CIP and the subcellular spatial resolution of microscopy. Notably, this technique measures unlabeled drug engagement, and, although not a direct measurement of drug concentration in the cell, we determined the engagement of drug to the target, which is ultimately the therapeutic objective. We quantitated intracellular target engagement of unlabeled covalent and reversible drugs in live cells in culture and *in vivo*.

RESULTS
Measuring binding with companion imaging probes
We hypothesized that an unmodified molecularly targeted drug would compete for target binding with a matched fluorescent CIP. Target engagement of the CIP, which is detectable by fluorescence polarization microscopy, would therefore be indicative of unlabeled drug binding. Detection was enabled by the large mass differences between the small fluorescent molecule in the free and protein-bound states (**Supplementary Results** and **Supplementary Fig. 1a**). With polarized light, only CIP molecules with absorption dipole moments aligned along the plane of excitation became excited through photoselection. Subsequent Brownian rotation of the excited molecules during the fluorescence lifetime was inversely related to the remaining polarization anisotropy of the emission photons. When bound to the target protein, CIP rotation slowed and the excited molecules retained orientation, producing polarization anisotropy. In the presence of unlabeled drug, however, the CIP could not bind as completely and the ensemble average polarization, representing the fraction of target bound CIP, became more isotropic, indicating unlabeled drug target engagement (**Fig. 1a**). To obtain spatial information, we imaged cells with polarized two-photon excitation light and collected

[1]Center for Systems Biology, Massachusetts General Hospital, Harvard Medical School, Boston, Massachusetts, USA. [2]Department of Systems Biology, Harvard Medical School, Boston, Massachusetts, USA. [3]Present address: Department of Molecular Science and Technology, Ajou University, Suwon, Korea. Correspondence should be addressed to C.V. (cvinegoni@mgh.harvard.edu) or R.W. (rweissleder@mgh.harvard.edu).
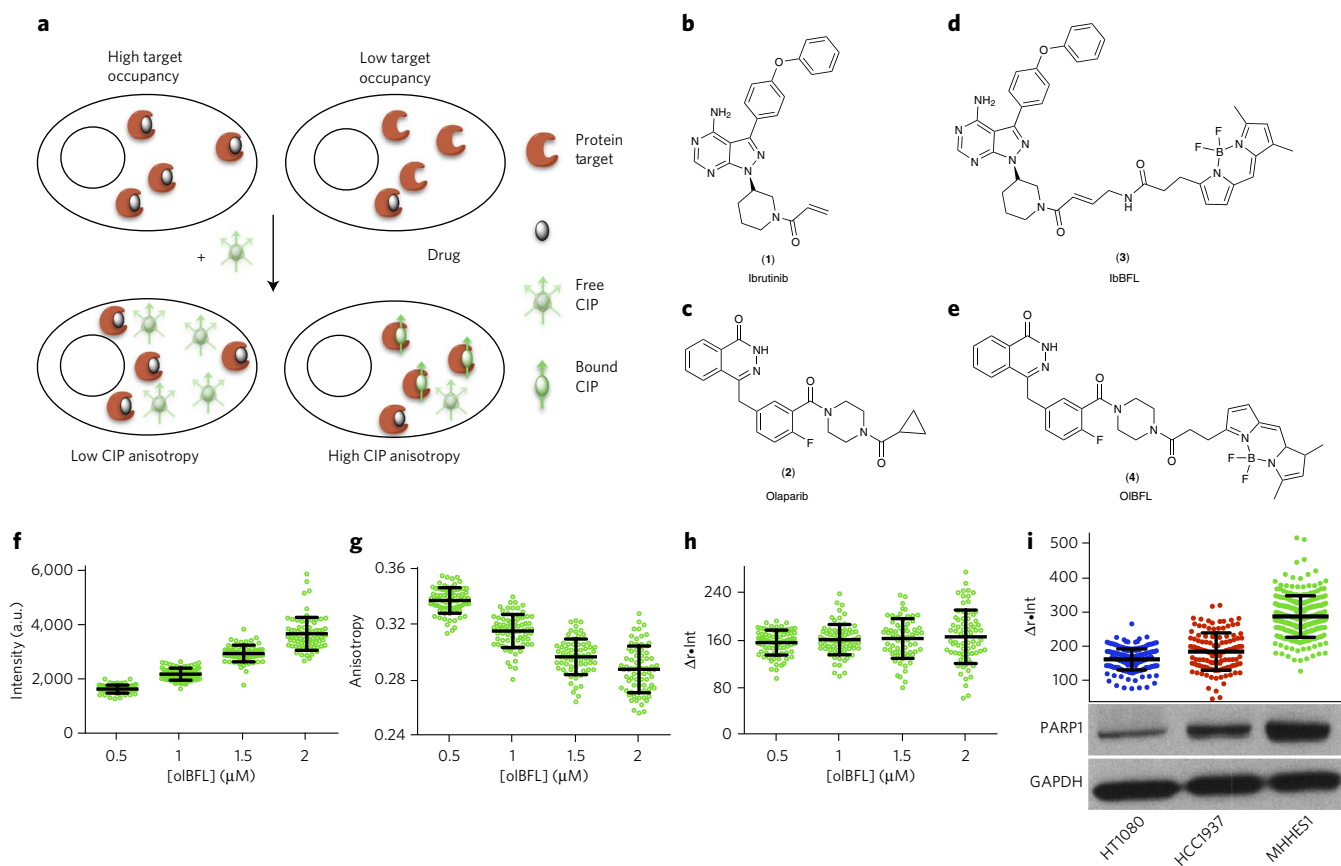
Figure 1 | Measuring single-cell drug binding through anisotropy competition imaging. (**a**) CIP measures unoccupied target through CIP rotational speed slowing when bound to the target, which increases the anisotropy and represents the degree of clinical drug target engagement. (**b**–**e**) Chemical structures of ibrutinib (**b**) and olaparib (**d**) and corresponding CIP linked to BODIPY-FL (**c**,**e**). (**f**–**h**) Single-cell HT1080 nuclei olBFL intensity (**f**), anisotropy (**g**) and $\Delta r \cdot \text{int}$ (**h**) incubated with different concentrations of olBFL. Data are presented as individual nuclei (green open circle) with mean ± s.d. (black), $n > 68$ per olBFL concentration, one technical replicate. (**i**) Single-cell nuclear $\Delta r \cdot \text{int}$ measurements of HT1080 (blue), HCC1937 (red) and MHHES1 (green). Data are presented as individual nuclei with mean ± s.d. (black), $n > 123$ per cell line, one technical replicate. Western blot (bottom) of HT1080, HCC1937 and MHHES1 cells for PARP1 (the most abundant PARP in the nucleus) and GAPDH. Full gels are shown in **Supplementary Figure 1**. PARP1 expression normalized to GAPDH is 1, 1.7 and 2.9 for HT1080, HCC1937 and MHHES1, respectively.

emission in channels parallel and perpendicular to the excitation polarization (**Supplementary Fig. 1b**).

As proof of principle, we focused on two different types of small molecule drugs: covalent irreversible inhibitors and reversible inhibitors. As an example of the former, we chose ibrutinib (**1**), a Bruton's tyrosine kinase (BTK) inhibitor[7]; as an example of the latter, we chose olaparib (**2**), a poly(ADP ribose) polymerase (PARP) inhibitor[20] (**Fig. 1b,c**). To obtain fluorescent CIPs of each drug (ibBFL (**3**) and olBFL (**4**)), we labeled them with BODIPY-FL using standard chemistries[21–23] (**Fig. 1d,e**).

Because anisotropy is an ensemble average of all excited fluorescent molecules it is dependent on the concentration of CIP in each measurement, which may not be uniform in complex *in vivo* settings. This phenomena was demonstrated by olBFL target engagement in HT1080 fibrosarcoma cell nuclei (**Fig. 1f–h**). At higher CIP concentrations, more unbound olBFL accumulated and the intensity increased, which decreased the anisotropy. Thus, nonspecific accumulation prevents measurement of total target engagement with intensity or anisotropy alone. We therefore derived a value, the difference in measured and unbound (nonspecific) anisotropy multiplied by the fluorescence intensity, $\Delta r \cdot \text{int}$ (**Online Methods**), which represents the concentration of CIP-bound target protein or uninhibited target. We indeed found that $\Delta r \cdot \text{int}$ is, unlike anisotropy or intensity, independent of CIP concentration under target-saturating conditions, with single-cell values that correlate with

primary target expression across three different cell lines (**Fig. 1i**). However, given that olaparib binds to PARP1–3 in the nucleus[24], the correlation is not unity. To assess the measurement sensitivity, we determined the coefficient of variation (COV) for measurement noise, nonspecific heterogeneity and target engagement heterogeneity of olBFL (**Supplementary Fig. 2**). We found a low COV for measurement noise (2%) and nonspecific heterogeneity (2.8%), but a high COV for target engagement heterogeneity (12%), indicating that measured heterogeneity largely arises from engagement heterogeneity across a population of cells.

Covalent inhibitors

Toledo cells, a B-cell lymphoma model expressing BTK, show high cytoplasmic ibBFL anisotropy. However, as expected, incubating Toledo cells with native ibrutinib for 20 min before ibBFL loading (**Supplementary Fig. 3a**) reduced the cellular CIP anisotropy in a concentration-dependent manner (**Fig. 2a**). To measure this change, we quantitated cytoplasmic $\Delta r \cdot \text{int}$ as a function of ibrutinib concentration (**Fig. 2b**) and found an intracellular ibrutinib K_i (50% engagement) of 2 nM, which was validated by traditional measurements (**Supplementary Fig. 3c**). We also extended our approach to another covalent BTK inhibitor, AVL292 (ref. 25), and quantitated binding constants using ibBFL as the CIP (**Supplementary Figs. 3d** and **4b**). However, with covalent inhibitors, target engagement depended on both the concentration and duration of exposure to
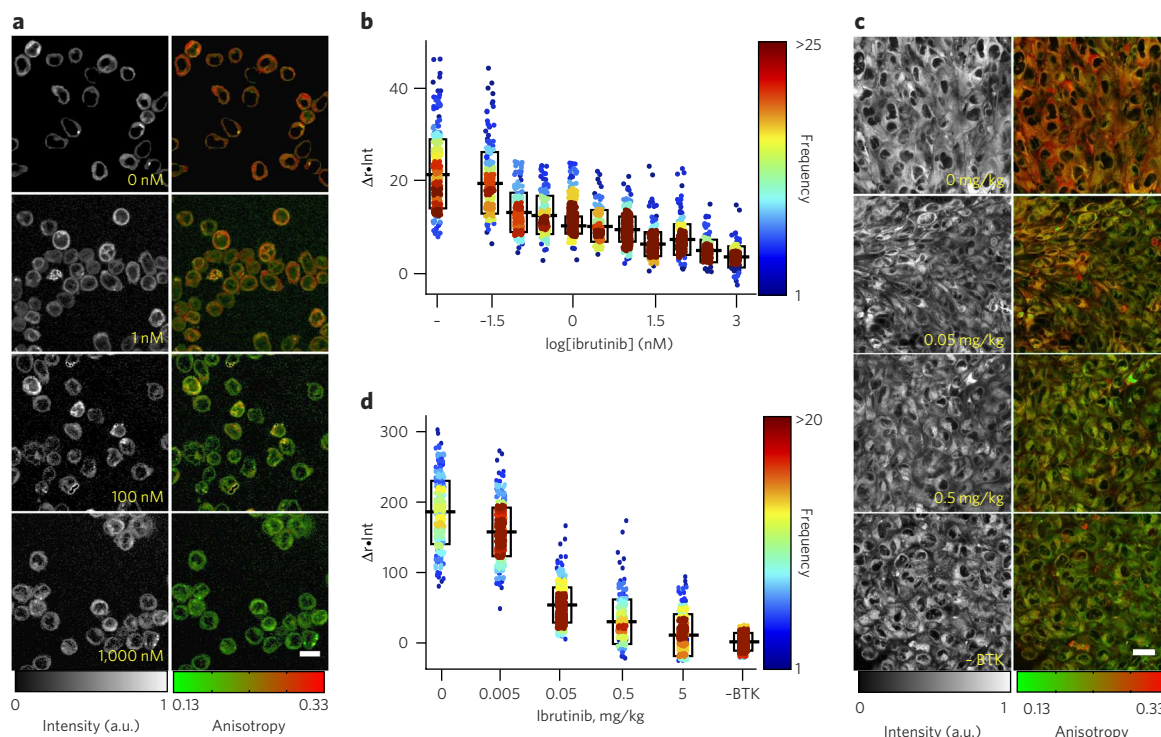
Figure 2 | Ibrutinib target engagement. (**a**) Representative CIP fluorescence intensity (left) and anisotropy (right) images of Toledo cells loaded with varying concentrations of ibrutinib (yellow) followed by ibBFL (150 nM). Scale bar represents 12 μm. (**b**) Single-cell Δr•int measurements of Toledo cells incubated with varying concentrations of ibrutinib for 20 min followed by ibBFL (150 nM). –, no ibrutinib. Shown are mean (black line) ± s.d. (black box), $n > 133$ cells per ibrutinib concentration, one technical replicate. Corresponding anisotropy measurements are shown in **Supplementary Figure 3e**. (**c**) Representative CIP fluorescence intensity (left) and anisotropy (right) images of HT1080 BTK-mCherry and BTK-free HT1080 H2B-mApple (bottom) tumors following systemic ibrutinib delivery (yellow) and *ex vivo* loading of ibBFL (200 nM). Scale bar represents 20 μm. (**d**) Single-cell Δr•int measurements of cell cytoplasm following systemic ibrutinib delivery and *ex vivo* ibBFL loading. Shown are mean (black line) ± s.d. (black box), $n > 200$ cells per ibrutinib concentration, one technical replicate. a.u., arbitrary unit.

the target, producing K_i values that were reliant on drug incubation time (**Supplementary Fig. 4a** and **Supplementary Table 1**). Thus, dynamic cellular properties that cannot be simulated *in vitro*, such as membrane penetration and compartmentalization inside the cell, will affect binding kinetics of these non-equilibrium drugs. After determining binding rate constants at each inhibitor concentration, we found that the intracellular second order binding constant (k_2/K_i), which also considers covalent activity, was higher for ibrutinib than for AVL292 (4.5×10^5 and 1.2×10^5 s^{-1} M^{-1}, respectively; **Supplementary Fig. 4c–e**).

To extend these measurements into the *in vivo* setting of complex tumor environments, we grew HT1080 tumors that were transfected with BTK-mCherry in nude mice. As expected, target engagement was dose dependent in these cells (**Supplementary Figs. 5** and **6**). To measure drug target engagement *in vivo* and accurately control exposure time, we administered ibrutinib intravenously, removed the tumor and incubated tissue in ibBFL (**Supplementary Fig. 7a**). CIP anisotropy was dependent on the ibrutinib dose delivered and allowed quantitation of ibrutinib target engagement in the tumor (**Fig. 2c,d**). Several factors contributed to the distribution of unoccupied target cellular levels: measurement noise (represented by BTK free tumor data; **Fig. 2d**), expression levels in single cells[26] and the distribution of ibrutinib in the tumor; the latter two dictate the level of engaged target and thus drug efficacy. To analyze total drug exposure *in vivo*, we compared average measurements to *in vitro* data (**Supplementary Fig. 7b**). Cytoplasmic measurements revealed cells with unoccupied target levels that might allow survival at otherwise effective concentrations (**Supplementary Fig. 7c**). For

example, at 1-h time points, average measurements indicated that 0.5 mg/kg intravenous ibrutinib was similar to ~3 nM constant exposure in cell culture, engaging 83% of total target in the tumor, yet 7% of the cells *in vivo* had unoccupied target levels that fell within the untreated tumor cell population.

Reversible inhibitors

We next investigated reversible small molecule inhibitor target engagement: a class of drugs that has proven to be particularly difficult to measure in cells and *in vivo* because of loss of equilibrium during sample processing and analysis. When olBFL was added to HT1080 cells expressing H2B-mApple, anisotropy was only high in the nucleus, where the majority of target PARP protein resides[24] (**Fig. 3a**). The presence of 1,000 nM olaparib reduced nuclear anisotropy values to cytoplasmic levels, indicating complete target occupancy by the unlabeled drug and specificity of the CIP for olaparib target. Notably, the spatial resolution of our approach enabled analysis on the nuclei only, which prevents errors that can occur in bulk measurements of accumulation arising from olaparib-independent CIP accumulation in the cytoplasm of cells. Punctate foci of olBFL binding in the nucleoli, where PARP has a higher abundance, were present in intensity-weighted anisotropy images. We found similar anisotropy values in foci and whole nucleus measurements, yet increased intensity and Δr•int, demonstrating the higher target concentrations (**Supplementary Fig. 8a–c**). Here, however, we analyze total nuclear signal to measure all PARP inhibitor target engagement in the nucleus. Quantitating cell nuclei Δr•int revealed a target engagement dose dependence (**Fig. 3b**), with greater heterogeneity at lower concentrations arising from target expression levels. We determined
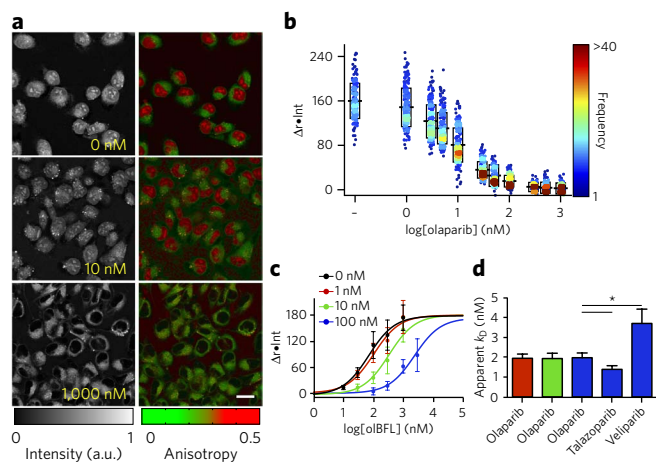
Figure 3 | Intracelullar PARP inhibitor target engagement.
(**a**) Representative CIP fluorescence (left) and anisotropy (right) images of intracellular olaparib activity *in vitro* in HT1080 H2B-mApple cells incubated with olaparib (yellow) and olBFL (500 nM). Scale bar represents 20 μm. (**b**) Single-cell nuclei Δr•int in HT1080 H2B-mApple cells *in vitro* incubated with olaparib and olBFL (500 nM). –, no olaparib. Shown are mean (black line) ± s.d. (black box), n > 187 cells per olaparib concentration, one technical replicate. Corresponding *in vitro* anisotropy measurements are shown in **Supplementary Figure 11a**. (**c**) Representative Schild curves of olBFL Δr•int in HT1080 cell nuclei in the presence of different olaparib concentrations. Data are total cell mean ± s.d., n = 3, with sigmoidal fit. (**d**) Apparent intracellular k_D of PARP inhibitors in HCC1937 (red), MHHES1 (green) and HT1080 (blue) cells (*$P < 0.05$, Student's *t* test). Data are mean ± s.d., n = 3.

the influence on drug resistance in PARP inhibitor target engagement (**Supplementary Fig. 9**). The activity of multidrug resistance protein 1 (MDR1) produced an 8.4- and 3.5-fold decrease in olaparib and talazoparib target engagement, respectively. Additionally, in separate experiments, although cells that were grown to resistance to olaparib displayed similar olaparib target engagement as control cells, they showed decreased target expression levels.

We also used Schild analysis[27], given the competition mechanism of olBFL (**Supplementary Fig. 8d–f**), to determine apparent intracellular k_D values for olaparib in HT1080 (1.97 ± 0.24 nM), HCC1937 (breast cancer, 1.93 ± 0.21 nM) and MHHES (Ewing's sarcoma, 1.92 ± 0.27 nM) cell lines, and found no significant difference across cell lines with different target expression levels (**Figs. 1i** and **3c,d** and **Supplementary Fig. 10**). However, we measured the apparent intracellular k_D of two other PARP inhibitors in HT1080 cells using olBFL and found that talazoparib had a higher affinity ($k_D = 1.38 \pm 0.18$ nM, $P < 0.05$), whereas veliparib has a lower affinity ($k_D = 3.68 \pm 0.72$ nM, $P < 0.05$), than olaparib (**Fig. 3d**), which correlates to previous non-cellular measurements[20,28,29] (**Supplementary Fig. 10f**). The similarity between intracellular and previous *in vitro* values demonstrate that NADH pocket targeting PARP inhibitors are quite specific inside cells.

We next determined PARP inhibitor intracellular activity in tumor models *in vivo* using HT1080 H2B-mApple xenograft tumors and intravital microscopy[30] (**Fig. 4a**). Administering drug and CIP locally to achieve a known concentration, we found similar olaparib target engagement *in vivo* as we did *in vitro* (**Supplementary Fig. 11b**). However, the cellular distribution of occupied target was much higher *in vivo* (average coefficient of variation at each concentration (except 1 μM) was 28 ± 14% higher; **Supplementary Fig. 11c**), potentially as a result of increased transcriptional heterogeneity that can occur *in vivo*[31]. Notably, we only analyzed cells with saturating olBFL (based on intensity) to ensure measurements were similar to *in vitro* conditions. Perhaps more relevant to clinical
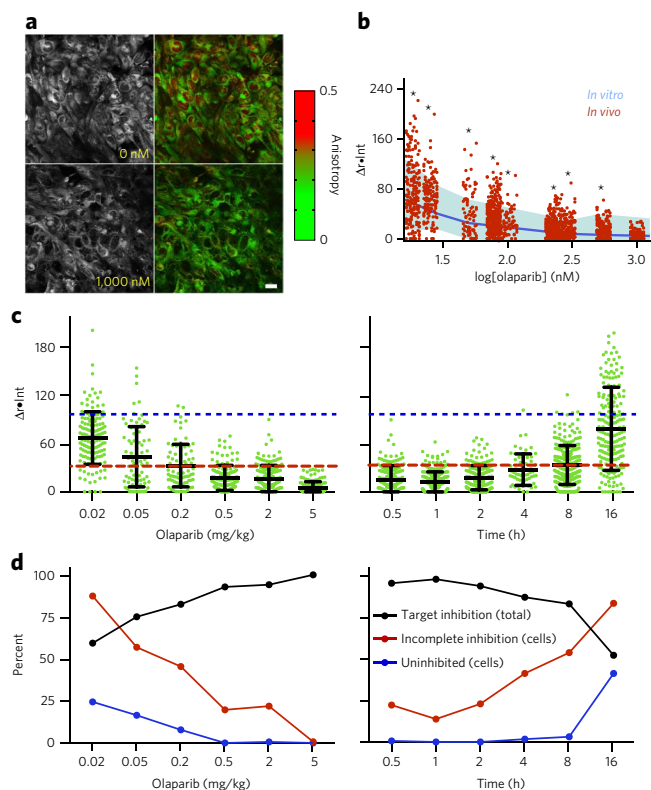

Figure 4 | *In vivo* olaparib target engagement. (**a**) Representative CIP fluorescence (left) and anisotropy (right) images of intracellular olaparib activity *in vivo* in HT1080 H2B-mApple cells incubated with olaparib (yellow) and olBFL (500 nM). (**b**) *In vivo* single-cell nuclei Δr•int (red) following systemic olaparib delivery (concentration determined from calibration; **Supplementary Fig. 11c**) with average (blue line) and range of (minimum to maximum, light blue) *in vitro* cell nuclei Δr•int measurements, n > 77 for each measurement, one technical replicate. * indicates significant ($P < 0.001$) difference in variance (F test) between *in vivo* and *in vitro* measurements, n = 1 measurement. (**c**) Single-cell nuclei Δr•int values of *in vivo* HT1080 H2B-mApple tumors 30 min after different olaparib concentration systemic (intravenous, i.v.) delivery (left) and at different times following systemic (i.v.) delivery of 2 mg/kg olaparib (right), n > 65 for each condition, one technical replicate. The red dashed line indicates 3 s.d. above the average Δr•int at 1 μM olaparib (**Supplementary Fig. 11b**) (99% confidence), the threshold above which intracellular target is not completely saturated by olaparib. The blue dashed line indicates the minimum cell nucleus Δr•int in absence of olaparib. (**d**) Data from (**c**) plotted over olaparib concentration (left and at different times (right). Percent of total target engagement (black), cell nuclei with incomplete engagement (red) and cell nuclei with unoccupied target levels within the range of untreated cell population.

pharmacokinetic strategies, heterogeneity was more pronounced following systemic delivery. Single-cell analysis revealed that *in vivo* olaparib target engagement was widely distributed around the *in vitro* average (using average, controlled *in vivo* data to determine drug concentration; **Supplementary Fig. 11c**), with unoccupied target heterogeneity that extended beyond *in vitro* measurements (**Fig. 4b**). For example, at 200 nM olaparib, average values revealed that the target was nearly saturated in both *in vitro* and systemic *in vivo* measurements, with little *in vitro* heterogeneity. However, a substantial fraction of tumor cells in animals treated systemically had unoccupied target levels outside the observed *in vitro* range, indicating that *in vitro* assays may not accurately represent *in vivo* conditions.

We then assessed target engagement dependency on dose and time after delivery (**Fig. 4c**). At lower doses and longer circulation times, the average target occupancy and the percentage of cells with complete target engagement were lower, whereas cellular distribution was higher (**Fig. 4c,d** and **Supplementary Fig. 11c**). Kinetic analysis of average values revealed an olaparib engagement half-life of 16.5 h (**Supplementary Fig. 11d**) following 2 mg/kg intravenous delivery. Following the same dose, comparison of average values to controlled measurements revealed that the overall olaparib concentration in the tumor was ~550 nM at 1 h, ~80 nM at 8 h and ~20 nM at 16 h (**Supplementary Fig. 11e**). However, single cell analysis showed that a subpopulation of cells had substantial unoccupied target at these high concentrations. For example, 2 h after intravenous 2 mg/kg administration, the measurement average revealed that all target was engaged, yet cellular analysis demonstrated that 25% of the cells had incomplete target occupancy. These results indicate that bulk measurements, such as plasma concentration, may not accurately represent drug binding in each targeted cell.

To be most effective, our approach needs to be sensitive and generalizable to other drugs. Using theoretical modeling, we found a limit of PARP detection for olBFL in the nucleus of 1.3 nM (**Supplementary Fig. 8i,j** and **Online Methods**). This limit was influenced by the affinity of olBFL and nuclear solubility of unbound olBFL (**Supplementary Fig. 8h**). In addition, to demonstrate the general applicability of our approach, we performed intracellular measurements of vinblastine (**5**), which is a clinically used tubulin binder, using a vinblastine CIP, vinBFL (**6**) (Online Methods)[32]. Single-cell uninhibited heterogeneity was more pronounced at higher vinblastine concentration than that seen with olaparib and ibrutinib. Tubulin concentration is likely more dependent on cell size and cycle than are PARP and BTK concentrations, which may explain the increased heterogeneity that we observed.

DISCUSSION
Currently, we can only infer target engagement through downstream, pharmacodynamic measurements or estimate it from measurements of bulk concentration in tissue. Both approaches are problematic, yet drug discovery science has depended on them. Thus, we are unable to analyze heterogeneous target engagement that may arise from cell cycle status[33], efflux pump expression[34], variable protein expression[35], the tumor microenvironment[36] or spatially heterogenous exposure through vasculature[37]. Our approach measures specific target engagement of unlabeled drug with high spatial resolution. The importance of measuring specific binding is well known in pharmacology research, and is emphasized by the high level of nonspecific interaction for the CIPs that we used (demonstrated by cytoplasmic olBFL intensity).

Our approach could be extended to other compounds and target classes using fluorophore attachment to amine-modified solvent exposed sites. However, binding affinity and competition with unlabeled inhibitors would first need to be determined for any new CIP. Furthermore, fluorescent labels must be chosen to ensure that CIPs localize intracellularly with the binding target[38]. CIP intracellular location may be more limiting for nuclear targets, as a fluorescent label could prevent nuclear permeability in live cells. To ensure accuracy in the measurements such that values can be compared across cell lines, the r_{min} value, or nonspecific interaction, for each cell type and CIP combination needs to be determined. This can be accomplished through analysis of target-free regions of a cell during CIP saturation or through measurements under unlabeled drug target saturation. In essence, nonspecific heterogeneity needs to be determined before a given CIP can be confidently employed.

With this approach the target engagement, or lack thereof, can be determined. Some inhibitors, however, have been shown to bind to multiple cellular targets with similar, or slightly decreased, affinities.

With these pan-target inhibitors, the relative abundance and affinity of each target will influence the target engagement of the clinical drug, and thus the measured engagement of the CIP. The sensitivity of our approach also depends on CIP affinity and target abundance. Notably, off target (targets that the CIP, but not the clinical drug engages) may also influence measurements.

Given that measurements are made on live cells, complimentary methods could be combined with our approach to develop a broader understanding of cellular pharmacology. For example, single-cell methods such as mass cytometry[39], RNAseq[40] or multi-target fluorescent immunohistochemistry (through cycle imaging)[41] would provide insight into how target engagement is effected by or affects RNA and protein expression, signaling, or location at the single cell level. However, measuring target engagement with our approach is limited by the need for a valid CIP and, currently, the use of window chambers for *in vivo* experiments (primarily to stabilize tissue). However, when using covalent drugs, tissue can be analyzed *ex vivo*. Existing alternative methods to determine target engagement do not provide single-cell resolution or work effectively using reversible inhibitors. Single-cell resolution not only provides information on the heterogeneity of target engagement, but allows measurements to be specific for cells of interest, omitting stromal or immune cells from being included in target engagement data. However, other approaches, such as CETSA[17], provide specific protein measurements through antibody detection. Otherwise, as the only method to measure single-cell target occupancy, this approach should be a valuable tool to better understand small molecule inhibitor target engagement.

METHODS
Methods, including statements of data availability and any associated accession codes and references, are available in the online version of the paper.

References
1. Bunnage, M.E., Chekler, E.L. & Jones, L.H. Target validation using chemical probes. *Nat. Chem. Biol.* **9**, 195–199 (2013).
2. Morgan, P. *et al.* Can the flow of medicines be improved? Fundamental pharmacokinetic and pharmacological principles toward improving Phase II survival. *Drug Discov. Today* **17**, 419–424 (2012).
3. Smith, D.A., Di, L. & Kerns, E.H. The effect of plasma protein binding on in vivo efficacy: misconceptions in drug discovery. *Nat. Rev. Drug Discov.* **9**, 929–939 (2010).
4. Mateo, J., Ong, M., Tan, D.S., Gonzalez, M.A. & de Bono, J.S. Appraising iniparib, the PARP inhibitor that never was–what must we learn? *Nat. Rev. Clin. Oncol.* **10**, 688–696 (2013).
5. Cohen, M.S., Hadjivassiliou, H. & Taunton, J. A clickable inhibitor reveals context-dependent autoactivation of p90 RSK. *Nat. Chem. Biol.* **3**, 156–160 (2007).
6. Gao, M. *et al.* Chemical genetics strategy identifies an HCV NS5A inhibitor with a potent clinical effect. *Nature* **465**, 96–100 (2010).
7. Honigberg, L.A. *et al.* The Bruton tyrosine kinase inhibitor PCI-32765 blocks B-cell activation and is efficacious in models of autoimmune disease and B-cell malignancy. *Proc. Natl. Acad. Sci. USA* **107**, 13075–13080 (2010).
8. Miller, M.A. *et al.* Tumour-associated macrophages act as a slow-release reservoir of nano-therapeutic Pt(IV) pro-drug. *Nat. Commun.* **6**, 8692 (2015).
9. Stadler, C. *et al.* Immunofluorescence and fluorescent-protein tagging show high correlation for protein localization in mammalian cells. *Nat. Methods* **10**, 315–323 (2013).
10. Simon, G.M., Niphakis, M.J. & Cravatt, B.F. Determining target engagement in living systems. *Nat. Chem. Biol.* **9**, 200–205 (2013).
11. Munteanu, B. *et al.* Label-free in situ monitoring of histone deacetylase drug target engagement by matrix-assisted laser desorption ionization-mass spectrometry biotyping and imaging. *Anal. Chem.* **86**, 4642–4647 (2014).
12. Lomenick, B. *et al.* Target identification using drug affinity responsive target stability (DARTS). *Proc. Natl. Acad. Sci. USA* **106**, 21984–21989 (2009).
13. Hargreaves, R.J. & Rabiner, E.A. Translational PET imaging research. *Neurobiol. Dis.* **61**, 32–38 (2014).

14. Fischman, A.J., Alpert, N.M. & Rubin, R.H. Pharmacokinetic imaging: a noninvasive method for determining drug distribution and action. *Clin. Pharmacokinet.* **41**, 581–602 (2002).

15. Matthews, P.M., Rabiner, E.A., Passchier, J. & Gunn, R.N. Positron emission tomography molecular imaging for drug development. *Br. J. Clin. Pharmacol.* **73**, 175–186 (2012).

16. Aboagye, E.O., Price, P.M. & Jones, T. *In vivo* pharmacokinetics and pharmacodynamics in drug development using positron-emission tomography. *Drug Discov. Today* **6**, 293–302 (2001).

17. Martinez Molina, D. *et al.* Monitoring drug target engagement in cells and tissues using the cellular thermal shift assay. *Science* **341**, 84–87 (2013).

18. Blum, G., von Degenfeld, G., Merchant, M.J., Blau, H.M. & Bogyo, M. Noninvasive optical imaging of cysteine protease activity using fluorescently quenched activity-based probes. *Nat. Chem. Biol.* **3**, 668–677 (2007).

19. Bachovchin, D.A., Brown, S.J., Rosen, H. & Cravatt, B.F. Identification of selective inhibitors of uncharacterized enzymes by high-throughput screening with fluorescent activity-based probes. *Nat. Biotechnol.* **27**, 387–394 (2009).

20. Menear, K.A. *et al.* 4-[3-(4-cyclopropanecarbonylpiperazine-1-carbonyl)-4-fluorobenzyl]-2H-phthalazin-1-one: a novel bioavailable inhibitor of poly(ADP-ribose) polymerase-1. *J. Med. Chem.* **51**, 6581–6591 (2008).

21. Turetsky, A., Kim, E., Kohler, R.H., Miller, M.A. & Weissleder, R. Single cell imaging of Bruton's tyrosine kinase using an irreversible inhibitor. *Sci. Rep.* **4**, 4782 (2014).

22. Thurber, G.M. *et al.* Single-cell and subcellular pharmacokinetic imaging allows insight into drug action *in vivo*. *Nat. Commun.* **4**, 1504 (2013).

23. Dubach, J.M. *et al.* In vivo imaging of specific drug-target binding at subcellular resolution. *Nat. Commun.* **5**, 3946 (2014).

24. Wahlberg, E. *et al.* Family-wide chemical profiling and structural analysis of PARP and tankyrase inhibitors. *Nat. Biotechnol.* **30**, 283–288 (2012).

25. Evans, E.K. *et al.* Inhibition of Btk with CC-292 provides early pharmacodynamic assessment of activity in mice and humans. *J. Pharmacol. Exp. Ther.* **346**, 219–228 (2013).

26. Roux, J. *et al.* Fractional killing arises from cell-to-cell variability in overcoming a caspase activity threshold. *Mol. Syst. Biol.* **11**, 803 (2015).

27. Arunlakshana, O. & Schild, H.O. Some quantitative uses of drug antagonists. *Br. J. Pharmacol. Chemother.* **14**, 48–58 (1959).

28. Shen, Y. *et al.* BMN 673, a novel and highly potent PARP1/2 inhibitor for the treatment of human cancers with DNA repair deficiency. *Clin. Cancer Res.* **19**, 5003–5015 (2013).

29. Donawho, C.K. *et al.* ABT-888, an orally active poly(ADP-ribose) polymerase inhibitor that potentiates DNA-damaging agents in preclinical tumor models. *Clin. Cancer Res.* **13**, 2728–2737 (2007).

30. Pittet, M.J. & Weissleder, R. Intravital imaging. *Cell* **147**, 983–991 (2011).

31. Dalerba, P. *et al.* Single-cell dissection of transcriptional heterogeneity in human colon tumors. *Nat. Biotechnol.* **29**, 1120–1127 (2011).

32. Meimetis, L.G. *et al.* Fluorescent vinblastine probes for live cell imaging. *Chem. Commun. (Camb.)* **52**, 9953–9956 (2016).

33. Niepel, M., Spencer, S.L. & Sorger, P.K. Non-genetic cell-to-cell variability and the consequences for pharmacology. *Curr. Opin. Chem. Biol.* **13**, 556–561 (2009).

34. Henneman, L. *et al.* Selective resistance to the PARP inhibitor olaparib in a mouse model for BRCA1-deficient metaplastic breast cancer. *Proc. Natl. Acad. Sci. USA* **112**, 8409–8414 (2015).

35. Spencer, S.L., Gaudet, S., Albeck, J.G., Burke, J.M. & Sorger, P.K. Non-genetic origins of cell-to-cell variability in TRAIL-induced apoptosis. *Nature* **459**, 428–432 (2009).

36. Trédan, O., Galmarini, C.M., Patel, K. & Tannock, I.F. Drug resistance and the solid tumor microenvironment. *J. Natl. Cancer Inst.* **99**, 1441–1454 (2007).

37. Minchinton, A.I. & Tannock, I.F. Drug penetration in solid tumours. *Nat. Rev. Cancer* **6**, 583–592 (2006).

38. Kim, E. *et al.* Optimized Near-IR fluorescent agents for in vivo imaging of Btk expression. *Bioconjug. Chem.* **26**, 1513–1518 (2015).

39. Spitzer, M.H. & Nolan, G.P. Mass cytometry: single cells, many features. *Cell* **165**, 780–791 (2016).

40. Wu, A.R. *et al.* Quantitative assessment of single-cell RNA-sequencing methods. *Nat. Methods* **11**, 41–46 (2014).

41. Lin, J.R., Fallahi-Sichani, M. & Sorger, P.K. Highly multiplexed imaging of single cells using a high-throughput cyclic immunofluorescence method. *Nat. Commun.* **6**, 8390 (2015).

Author contributions

J.M.D., C.V. and R.W. designed the experiments. E.K. and L.G.M. synthesized CIPs. E.K. performed in-gel experiments. J.M.D., K.Y. and R.J.G. performed cell experiments. J.M.D. performed *in vivo* experiments. J.M.D. and M.C. analyzed data. J.M.D. and C.V. performed imaging experiments. J.M.D. and R.W. wrote the paper, and all of the authors reviewed and approved the final manuscript.

Competing financial interests

The authors declare no competing financial interests.

Additional information

Any supplementary information, chemical compound information and source data are available in the online version of the paper. Reprints and permissions information is available online at http://www.nature.com/reprints/index.html. Correspondence and requests for materials should be addressed to C.V. or R.W.

ONLINE METHODS

Cell culture. HT1080 cells (ATCC) stably expressing BTK-mCherry[21] were cultured in DMEM supplemented with 10% FBS and 1% Pen/Strep (Invitrogen). Virus generated from pMSCVpuro-BTK-mCherry retroviral vector was a generous gift from H. Ploegh (Massachusetts Institute of Technology). Viral supernatant was added directly to HT1080 cells for 48 h, and BTK-mCherry-expressing cells were then selected with DMEM media containing 2 μg/mL puromycin for 96 h. HT1080 MDR cells were constructed using components of the MDR1 expression plasmid (Addgene, plasmid no. 10957: pHaMDRwt) and a lentiviral vector pLVX (Clontech)[42]. HT1080 cells stably expressing H2B-mApple (addgene) were cultured in DMEM supplemented with 10% FBS and 1% Pen/Strep under geneticin (100 μg/ml, Invitrogen) selection. Toledo (B lymphocytes, ATCC), MHHES1 (Ewing's sarcoma, CLS Cell Line Services), UWB1.289 (cervical cancer, ATCC) and HCC1937 cells (breast cancer, kind gift of T. Mitchison, Harvard Medical School) were cultured in RPMI (Invitrogen) with 10% FBS and 1% Pen/Strep. Cells were imaged in phenol red free DMEM (Invitrogen) with 10% FBS and 1% Pen/Strep. All cell lines tested negative for mycoplasma before use and at the end of experiments.

CIPs. ibBFL[21], olBFL[22] and vinBFL[37] were synthesized as previously described. A detailed analysis is in the **Supplementary Note**.

In vitro cell experiments. *Non-adherent cell experiments.* Toledo cells (ATCC) ($\sim$5 × 10^4) were centrifuged in 1 ml volumes (300 *g* for 3 min), resuspended in the desired concentration of BTK inhibitor and incubated in a cell incubator (37 °C and 5% CO$_2$) in 12-well plates. Following incubation, cells were centrifuged and washed once to removed unbound drug. Cells were resuspended in 1 ml of RPMI containing 150 nM ibBFL and returned to the incubator for 3 h. The 3 h incubation time was used to ensure complete binding of ibBFL (**Supplementary Fig. 3b**). Cells were then centrifuged and resuspended in 50 μl of phenol-red free media containing 150 nM ibBFL. Cells (10 μl) were then transferred to a microscope slide, covered with a no. 1 cover glass and imaged in the presence of ibBFL. As a control (no BTK expression) we delivered spCAS9 and the guide RNA CTTACCGGAATCTGTCTTTC using a lentiviral approach (GenScript) to Toledo cells. However, knockout of BTK proved to be lethal. We thus used used HT1080 H2BmApple cells (known to have very low BTK levels) and compared them to HT1080 BTKmCherry cells (high BTK levels) to better characterize BTK inhibitor engagement.

HT1080 BTKmCherry cell experiments. Cells were grown to ~75% confluency on 12-mm glass coverslips in 12-well plates. To determine the binding rate of ibBFL the CIP was added at 250 nM in phenol red free media and the cells were returned to the incubator. Cells were removed at 30 min intervals and imaged in the presence of incubation media with ibBFL. For intensity of bound drug experiments ibrutinib was added at 20 nM in media for various times. The drug was then washed off and ibBFL was added at 250 nM for 3 h to ensure complete binding of ibBFL (**Supplementary Fig. 3b**). The cells were then washed in phenol red free media for 18 h and imaged. To determine the binding affinities of BTK inhibitors in HT1080 BTK-mCherry cells, drug was added at the desired concentration and the cells were returned to the incubator for the desired time. Media was then removed, the cells were washed once with drug free media, and phenol red free media containing 250 nM ibBFL was added to each well. The cells were then returned to the incubator for 3 h before imaging in the presence of incubation media with ibBFL, to ensure complete binding the CIP (**Supplementary Fig. 3b**).

PARP inhibitor experiments. HT1080, HCC1937 or MHHES1 cells were grown to ~75% confluency on 12-mm cover glass in 12-well plates. PARP inhibitor and olBFL, at the desired concentrations, were brought up in phenol-red-free media from 10 mM DMSO stocks and added to the cells. The cells were then incubated for 20 min and transferred to the microscope for imaging in incubation media with olBFL.

Resistance. HT1080 MDR cells were grown to ~75% confluency on 12-mm cover glass in 12-well plates. Olaparib was added at the desired concentration for 30 min in the presence or absence of 1 μM tariquidar (SelleckChem). The cells were then washed and 1000 nM olBFL was added in the presence of 1 μM tariquidar for 15 min. Cells were immediately transferred to the microscope for imaging. UWB1.289 cells were created resistant to olaparib by increasing

olaparib in the growth media from 20 nM to 1 μM over the course of a month while maintaining a sub-confluent population. Viability response to olaparib was determined through the presto blue assay following manufacturer's directions (Life Technologies).

Western blot. Cells were grown to confluence, washed twice with ice-cold PBS and then lysed in RIPA with protease inhibitor. Lysates were passed through a 23g syringe, incubated for 5 min on ice, sonicated for 1 min and centrifuged at 14,000 *g* for 15 min at 4 °C to remove cellular debris. Total protein was measured using the BCA assay (Pierce) and equal protein was loaded on a 4–12% NuPAGE Bis-Tris gel (Life Technologies). The blot was blocked in SuperBlock T20 (TBS) (Pierce) for 1 h, followed by brief washing in TBS containing 0.1% Tween-20 (TBST). Blots were incubated overnight at 4 °C in PARP1 (9532, Cell Signaling Technology) primary antibody diluted 1:1,000 in 10% SuperBlock/TBST. Blots were washed three times, 5 min each, followed by a 1-h incubation in HRP-conjugated secondary antibody 1:2,000 in 10% SuperBlock/TBST. Blots were again washed three times, 5 min each in TBST followed by detection using SuperSignal West Pico chemiluminescent substrate (Pierce). Blots were stripped with restore western blot stripping buffer (Thermo) and staining was repeated with GAPDH (AF5718, R and D Systems) primary antibody.

Animal experiments. All animal experiments were approved by the Massachusetts General Hospital Institutional Animal Care and Use Committee. Animals (Female, 20-week-old nude mice (Cox-7, Massachusetts General Hospital)) were anesthetized with 2% isoflurane in oxygen at a flow rate of 2 l/min for both surgical and imaging procedures. All surgical procedures were performed under sterile conditions. The body temperature of mice was maintained at 37 °C during surgical and imaging procedures. Between one and three animals were used per condition. If multiple animals were used, the average cell values of each measurement were within 10% to eliminate artifacts in heterogeneity. Animals were excluded if no tumors were visible via fluorescent protein expression. No randomization was performed and the experimenter was not blinded.

For ibrutinib experiments, nude mice were injected subcutaneously with 10^6 HT1080 BTK-mCherry or HT1080 H2B-mApple cells in 50 μl of PBS on both sides of the flank. Once the tumors reached at least 100 mm^3 (14–21 d), ibrutinib was injected i.v. through the tail vein (30 gauge needle). Ibrutinib (10 mM in DMSO) was diluted first in DMSO to 10 μl volume, then diluted in 10 μl of 1:1 DMAC:Solutol and further diluted in PBS to reach the desired concentration in 100 μl volume. 1 h after injection, the animals were sacrificed and perfused with 10 ml of PBS through the left ventricle to flush residual blood from the tumor. The tumors were removed and incubated in 200 nM ibBFL in DMEM media supplemented with 10% FBS and 1% pen/strep for 3 h in a cell incubator before imaging. Lectin-fluorescein (Vector Labs) was injected i.v. 30 min prior tumor removal to image the vasculature.

For olaparib experiments, dorsal window chambers were implanted on nude mice and HT1080 H2B-mApple cells were injected into the skin fascia, 5 × 10^5 cells in 50 μl of PBS. Tumors were allowed to grow for at least 10 d. To determine binding, the glass cover slip was removed from the window and olaparib and olBFL were added topically at the desired concentrations in sterile PBS. Images were taken after 20 min to allow for diffusion and binding equilibrium. For systemic measurements olaparib (10 mM in DMSO) was diluted first in DMSO to 10 μl volume, then diluted in 10 μl of 1:1 DMAC:Solutol and further diluted in PBS to reach the desired concentration in 100 μl volume. The drug was then delivered i.v. through the tail vein (30 gauge needle). 20 min before imaging the cover glass of the chamber was removed and 500 nM olBFL in PBS was added topically.

Data analysis. Images were analyzed in ImageJ, Matlab, and Prism. The detector noise was first removed and the anisotropy, total fluorescence, and Δr•int were then calculated at each pixel. Regions of interest were used to define cells and subcellular compartments and the average anisotropy and intensity of each region was then determined. Data were transferred to Prism where all curve fitting was performed. De-noised images were created in Matlab and anisotropy images were generated using a custom look up table. Single-cell dose

response data were binned into groups based on anisotropy or Δr•int value, the number of cells in each bin was then used to assign a color based on a jet look up table.

To analyze PARP inhibitor cell data, nuclei were segmented using the H2B-mApple fluorescence channel. The average intensity and anisotropy in each nucleus was then calculated. For *in vitro* experiments the minimum anisotropy (r_{min}) was determined by segmenting multiple cell cytoplasms and finding the average value for each cell type used. For *in vivo* experiments, the intensity and anisotropy of each cell cytoplasm were measured by assigning a region adjacent to the cell nucleus. The cytoplasmic anisotropy was used to determine r_{min} for each cell, which normalizes the measurement for any scattering artifacts. Additionally, the cytoplasmic intensity was used to ensure olBFL had saturated the cells. Cells in which olBFL intensities were below the 1.2 times the average intensity of saturation, derived from **Figure 1f**, were omitted from analysis. If cytoplasmic values of anisotropy were below 0.22 or the intensity was too low, the cell nucleus was not considered for analysis.

To analyze BTK inhibitor data in Toledo cells, cells were segmented to remove cell debris and dead or dying cells. The average intensity and anisotropy in each cell cytoplasm was then calculated. To analyze HT1080 BTK-mCherry cells *in vitro* and *ex vivo*, cells were segmented using the empty nucleus and mCherry channel. The average BODIPY FL channel fluorescence and anisotropy and mCherry intensity were then found for each region. The minimum anisotropy (r_{min}) was determined by segmenting the cytoplasm of HT1080 H2B-mApple cells loaded with ibBFL, and average value of 0.23 was found. For *ex vivo* measurements the intensity was used to confirm cell saturation.

Ex vivo tumor images were created from 2 micron section z-stacks using a 20× water objective in both confocal (fluorescein and mCherry) and two-photon (SHG) modes. The images were processed using Amira software (FEI).

Statistical analysis. Student's *t* test and F tests were performed when necessary in Excel and Prism.

Imaging. Images were taken on an Olympus BX61-WI upright microscope with two-photon excitation adapted to make polarization measurements as previously described[23]. Briefly, a Glan-Thompson polarizer and half wave plate were inserted in the excitation laser line (MaiTai DeepSee Ti:sapphire pulsed laser (Spectra Physics) with a pulse width of 110 fs and a repetition rate of 80 MHz) to polarize the excitation light. Emission was collected through a 690-nm short-pass filter. Light was split with a 570-nm dichroic mirror and filtered through emission bandpass filters (495–540 nm) and (575–630 nm). Green emission (BODIPY FL) was split into orthogonal polarizations with a polarizing beam splitter in a custom filter cube and detected with photomultiplier tubes (PMT). The PMT gains were adjusted such that 2 μM fluorescein in water produced an anisotropy of 0.004 at 25 °C. The alignment and measured intensity of the system was tested before each experiment using fluorescent calibration slides and adjusted if necessary. Images were acquired at 910-nm excitation through a 25× 1.05 NA water immersion objective (XLPlan N, Olympus). Laser power was constant throughout experiments. Confocal images were taken with 2× 0.14 NA (XFluor, Olympus) and 20× 1.00 NA water immersion (XLUMPlan FL N, Olympus) objectives. Second harmonic generation images were taken in two-photon with 880 nm excitation and emission collected between 420–460 nm with a 20× 1.00 NA water immersion objective.

The intensities of each image were determined through summation of the intensity of each polarization channel at each pixel. Fluorescence anisotropy at each pixel was calculated from the equation: $r = (I_{\parallel} - I_{\perp}) / (I_{\parallel} + 2I_{\perp})$, where r is anisotropy, $I_{\parallel}$ is the intensity in the parallel channel and $I_{\perp}$ is the intensity in the perpendicular channel. A custom look up table was generated for each CIP to assign color to anisotropy value. Images were cropped to remove polarization artifacts at the edges. For visualization, the anisotropy color image was weighted by the intensity image.

ibBFL binding experiments. Purified BTK (Promega) was diluted in PBS to a concentration of 1 μM. ibBFL was diluted from a 10 mM stock in DMSO to 1 μM in phenol-red-free media. Solutions were then created from the two stocks to have a concentration of 500 nM ibBFL and varying concentrations of BTK

(0–600 nM) with volume made up with PBS. 5 μl of solution was then trapped between two spaced pieces of cover glass and imaged. Therefore, ibBFL concentration was constant across the binding curve.

BTK in-gel fluorescence. Toledo cells (3×10^6 per ml, 1 mL) were incubated with different concentrations of Ibrutinib and AVL292 in growth media (ranging from 25 to 0.025 μM). After 20 min incubations, cells were washed once with growth media and incubated with 150 nM ibBFL solution in growth media at 37 °C 5% CO_2 incubator for 3 h with gentle mixing at every hour. After incubation, cells were washed with ice-cold PBS 1X and then lysed with 100 μl of radioimmunoprecipitation buffer (RIPA, Cell Signaling Technology) containing HALT protease inhibitor cocktail (Pierce) on ice for 1 h with gentle vortexing every 20 min. After incubation, each tube was centrifuged at 10,000g for 10 min at 4 °C and cell lysate in supernatant was obtained. Protein concentration of cell lysates was quantified with BCA protein assay (Pierce) and were brought to the same concentration by dilution with 1× RIPA buffer (Cell Signaling). Resulting cell lysates were mixed with NuPAGE LDS sample buffer (Life Technology) and heated at 85 °C for 5 min. 20 μl of sample per lane was loaded onto a 12-well NuPAGE Novex 4–12% Bis-Tris gels (Invitrogen). Gels were run in NuPAGE MES SDS running buffer (Life Technology) at 200 V for 35 min in the XCell SureLock Mini-Electrophoresis system (Invitrogen). The gels were removed from the cassette and fluorescent intensity of each band was measured using a Typhoon 9410 fluorescent scanner (GE Healthcare) using 488-nm excitation and 520-nm emission filter. Fluorescent intensity was quantified using ImageJ.

Schild analysis. Sigmoidal curve fits (Prism) were used to find the IC50 of the olBFL binding curve for each concentration of PARP inhibitor. These values were then used to create dose ratios (IC50 at a given PARP inhibitor concentration divided by the IC50 when no PARP inhibitor is present). The log of the dose response minus one was plotted against the log of the PARP inhibitor concentration. A linear line with a slope equal to one was then fit to the data and the y intercept ($y = 0$) was used to determine the apparent intracellular k_D.

Derivation of Δr•int. Anisotropy is defined by the Perrin equation[43]

$$\frac{r_o}{r} = 1 + \frac{\tau}{\tau_\theta} \tag{1}$$

where r is the anisotropy, r_o is the fundamental anisotropy (no rotation) of the molecule, dictated by the angle between the absorption and emission dipole moments, τ is the fluorescence lifetime and $\tau\theta$ is the rotational lifetime. Assuming fluorescence lifetime is constant[21], when a fluorescent drug binds to the much larger protein target the rotational lifetime increases and the anisotropy becomes closer to the fundamental anisotropy.

Anisotropy is an ensemble measurement representing the average of all molecules within the measured sample or volume. This can be represented by

$$r = \sum_{n=1}^{i} \frac{r_n N_n}{N_{tot}} \tag{2}$$

where r_n is the anisotropy of a given state, N_n is the number of molecules in that state and N_{tot} is the total number of fluorescent molecules measured. For the system of a fluorescent drug binding to the protein target there can exist two molecular states, bound and unbound. Here, we assume that off target effects are minimal and thus do not represent a potential third state. This assumption is validated by the lack of non-specific heterogeneity of a CIP, discussed below.

The two state system can be represented by

$$r = \frac{r_{bound}[RD_{fluo}] + r_{free}[D_{fluo}]_{free}}{[D_{fluo}]_{tot}} \tag{3}$$

where r_{bound} is the anisotropy value of bound CIP, $[RD_{fluo}]$ is the concentration of bound CIP, r_{free} is the anisotropy value of unbound CIP, $[D_{fluo}]_{free}$ is the concentration of unbound CIP, and $[D_{fluo}]_{tot}$ is the total concentration of CIP.

The total CIP in the measurement is the sum of the two states, bound and unbound

$$[D_{fluo}]_{tot} = [D_{fluo}]_{free} + [RD_{fluo}] \tag{4}$$

Equations (3) and (4) can be rearranged to

$$[RD_{fluo}] = \frac{r - r_{free}}{r_{bound} - r_{free}}[D_{fluo}]_{tot} \tag{5}$$

Assuming minimal photobleaching and a linear relationship across the measurement range, the total fluorescence drug concentration can be related to the measured intensity through the constant γ:

$$Int = \gamma[D_{fluo}]_{tot} \tag{6}$$

Substituting equation (6) into equation (5) we get

$$[RD_{fluo}] = \frac{r - r_{free}}{r_{bound} - r_{free}}\frac{Int}{\gamma} \tag{7}$$

Finally, grouping constants into a single term, C, equation (7) can be rearranged into

$$C = \frac{1}{\gamma(r_{bound} - r_{free})} \tag{8}$$

or

$$[RD_{fluo}] = C(r - r_{free})Int \tag{9}$$

$$[RD_{fluo}] = C \cdot \Delta r \cdot Int \tag{10}$$

Here, the difference between the measured anisotropy and the unbound anisotropy, a constant, multiplied by the intensity has a linear relationship to the concentration of bound fluorescent drug through the constant C.

Under target saturation conditions in the absence of any other inhibitors, $\Delta r \cdot int$ represents the total amount of target. This relationship is demonstrated in **Figure 1f,h**. The nuclear intensity of HT1080 cells loaded with olBFL increases with increasing fluorescent drug concentration. However, the increasing intensity arises from unbound fluorescent drug in the nucleus, which produces a lower measured anisotropy signal. Yet, $\Delta r \cdot int$ is independent of the olBFL concentration. Therefore, the total target concentration is $\Delta r \cdot int$ multiplied by the constant C.

Limit of detection. Because our approach relies on the stoichiometric engagement of CIP to target there will be a limit of detection that depends on the CIP affinity and target expression levels. For covalent inhibitors the limit is theoretically one target copy number, as the affinity goes to infinity over time. For reversible inhibitors, the detection limits are higher. Specifically, the detectable expression level depends on the amount of CIP added. Two opposing factors dictate the detection limit: the measurable difference in anisotropy and saturation of the target with the CIP. Higher CIP concentrations will more likely saturate the target, yet provide more unbound CIP thus reducing the measured anisotropy.

For olBFL we found a theoretical limit of detection in the nucleus of 1.3 nM of protein target when 50 nM olBFL is applied to cells (**Supplementary Fig. 8i,j**). At this olBFL concentration and 1.3 nM of target, the Δr is above measurement noise yet the difference in $\Delta r \cdot int$ and saturated $\Delta r \cdot int$ is below measurement noise. This limit of detection is determined by the affinity of

olBFL for the target and the solubility of unbound CIP in the nucleus. However, if olBFL had a decreased affinity the limit of detection would be higher. To make target engagement measurements the expression levels of the target need to be higher than the limit of detection. Therefore, low affinity CIP may not be capable of detecting low abundance target and drug engagement.

We validated anisotropy dependence on binding of ibBFL with pure BTK protein in solution (**Supplementary Fig. 1c**). At constant ibBFL (500 nM) increasing concentration of BTK increased the imaged anisotropy. The anisotropy value plateaued at 500 nM when ibBFL was saturated by the target protein. Binding of olBFL was previously demonstrated[21].

Multiple targets. Drugs that bind to multiple targets with high affinity will produce target engagement measurements that reflect the average engagement across all target. It is not possible to distinguish engagement to one protein species from another. That is, however, unless the size of the targets are significantly (>~2 orders of magnitude) different. The anisotropy of CIP engaged to different sized targets may be different, as anisotropy is imparted by the rotational speed of the target. Therefore, different targets rotating at different rates would introduce a third anisotropy state into the measurement. However, because most proteins are within a couple orders of magnitude the anisotropy differences between CIP bound to different proteins in negligible. If the drug engages other macromolecular targets, such as mRNA, as well as protein the differences could influence the measurements.

Off target effects. Since anisotropy is an ensemble average of all states in the system it is important to establish that only two states are present for equation (3) to be valid. The target engaged CIP is one state, while non-specific, or unbound, is the second state. Off target binding or a non-selective CIP would represent a third state. However, these additional states can be assumed to constituent a single unbound state if the heterogeneity of the unbound measurements is low. A single unbound state integrates all the non-specific interactions of the CIP inside a cell. If the measured anisotropy is similar amongst a population of cells than these non-specific interactions can be removed. The resulting target engagement values represent only what the unlabeled drug engages. Any heterogeneity in the non-specific anisotropy above the error of measurement would prevent the reliable removal of the unbound fraction of CIP from target engagement values and thus produce inaccurate results. Therefore, the CIP non-specific anisotropy (r_{min}) heterogeneity needs to be determined for each CIP-cell combination. Here we found similar r_{min} values that were independent for cell type for each CIP used (0.24 and 0.23 for olBFL and ibBFL, respectively).

Generality of approach to different experimental systems. Once off target effects have been determined and ruled out as potential contributors to measurement noise, the use of $\Delta r \cdot int$ provides a means to compare measurements between experimental systems (for example, different microscopy setups). However, because $\Delta r \cdot int$ incorporates the intensity of the measured signal, only relative differences between conditions can be compared across systems. For example, $\Delta r \cdot int$ provides an approach to determine the apparent intracellular k_D of a drug through measurements at different CIP and drug concentrations using Schild analysis (**Fig. 3** and **Supplementary Fig. 10**). Anisotropy is an absolute measurement and should be directly comparable between systems. However, anisotropy cannot be used to determine k_D because of the competitive binding mechanism (**Supplementary Fig. 8e**).

42. Laughney, A.M. *et al.* Single-cell pharmacokinetic imaging reveals a therapeutic strategy to overcome drug resistance to the microtubule inhibitor eribulin. *Sci Transl. Med.* **6**, 261ra152 (2014).

43. Perrin, F. The polarisation of fluorescence light. Average life of molecules in their excited state. *J. Phys. Radium* **7**, 390–401 (1926).